scientific reports

Check for updates

OPEN

Harvesting of flow current through implanted hydrophobic PTFE surface within silicone-pipe as liquid nanogenerator

Ravi Kumar Cheedarala✉ & Jung Il Song✉

Harvesting of flow current through implanted hydrophobic surface within silicone pipe as liquid nanogenerators where Tap water (TW), and DI water (DIw) as liquid reservoirs to successfully convert induced mechanical energy into electrical energy. Here, we used a commercial PTFE film for the generation of a hydrophobic surface as a source of mechanical energy. The surface roughness of the hydrophobic surface is confirmed using atomic force microscopy, and contact angle analyses. The generation of power through the interaction of TW and DI with inbuilt PTFE in silicone tube is described. The higher output voltage (V*oc*), and short circuit currents (I*sc*) were attained through an interaction of TW and DIw with N-PTFE. The lower V*oc*, and I*sc*'s were produced when DI water interacts with N-PTFE electrode, whereas TW produced higher V_{oc} and $I_{sc's}$, respectively, due to a lack of free mobile ions in DIw than TW. The TW-Sh-TENG and DIw-Sh-TENG are produced the maximum peak-to-peak Voc, and Isc of 29.5 V and 17.4 V and 3.7 µA, and 2.9 µA, respectively. Significant power output enhancement of ~ 300% from TW-Sh-TENG from DIw-N-TENG due to the formation of higher surface roughness and lead to the slipping of water droplets by super-hydrophobicity.

Triboelectric nanogenerators (TENGs) can harvest energy from different sources in the environment, including mechanical vibration, heat, tides, and wind[1–6]. Also known as triboelectrification, contact electrification involves surface charge transfer when materials with two different polarities are brought into contact. Various triboelectric mechanisms have been developed using tidal and wind energy to generate mechanical vibration, as well as human movement, muscle stretching, and air and water flow[7–10]. There are many potential applications, such as energy harvesting, chemical sensors, electrostatic-charge patterning, metal-ion detection, and laser printing[11–13].

A solid TENG is based on solid–solid contact electrification in dry weather, but the efficiency is gradually ruined due to the increasing effect of friction, which damages the effective-contact surface area and decreases the triboelectric charge output due to nano- to micrometer patches between the two solid electrodes[14,15]. Besides, solid–solid contact TENGs become saturated because of the lack of accessibility of surface destruction that could occur with flexible materials[2,16]. It is difficult to examine the yielding power at the nano-level, which defines the point where the material structure begins to change (elastic + plastic) nonlinearly. Therefore, there are currently many technologists focusing on the development of solid–liquid contact TENGs for generating high triboelectricity. But the development of an effective solution for this problem remains a challenging task, and the approaches are expensive and complex[17,18].

Lin et al. reported a triboelectric charge with an open-circuit voltage (V_{oc}) of up to 52 V and short-circuit current (I*sc*) density of 2.45 mA/m^2 from water-TENG contact electrification[19]. Niu et al. developed the theory and the working mechanism of a sliding-mode TENG for both energy scavenging and self-powered sensor applications[20]. In another work, water drop energy was harvested by a sequential contact-electrification and electrostatic-induction process, and the output current and power density were 1.5 µA/cm^2 and 20 mW/cm^2 from tap water, respectively[21]. Tang et al. reported a mercury-based high-performance TENG with immediate energy-conversion efficiency using Kapton, copper electrodes, and mercury as the friction materials[18]. Recently, Zhao et al. were developed an ultrahigh electricity generation from low-frequency mechanical energy by efficient energy management and they produced over 7.5 kV energy through TENGs[22]. Besides, Yike et al. have been reported independent TENG results based on air-break down model charge excitation triboelectric nanogenerators and received the charge density of 2.38 m C/m^2 using 4 µm thickness PEI film[23]. However, the focus

Department of Mechanical Engineering, Research Institute of Mechatronics, Changwon National University, Changwon City, Republic of Korea. ✉email: ravi@changwon.ac.kr; jisong@changwon.ac.kr

of previous studies has been the enhancement of energy conversion rather than eco-friendliness and human health, especially regarding the central and peripheral nervous systems, which are serious considerations for environmental and living systems.

Zhu et al. developed a water-wave energy-harvesting system by an asymmetric screening of electrostatic charges on a nanostructured hydrophobic thin-film surface. The main focus was the liquid–solid electrification-enabled generator, which is based on a fluorinated ethylene-propylene thin film and free-standing-mode water, and a basic comparison with other modes was not performed[24]. Recently, our group reported sustainable green current generated by a fluid-based TENG (FluTENG) and compared contact and sliding modes using PTFE as an electrode. The triboelectric-power density values were 2.15 mW/m^2 and 0.8 mW/m^2 for the CS-FluTENG and LS-FluTENG, respectively[21,24]. Very recently, Yang et al. reported a water tank TENG fabricated with super-hydrophobic PTFE for efficient harvesting of water-wave energy using tap water, DI water, and NaCl solutions in reservoirs. The triboelectric open-circuit voltage (V_{oc}) and short-circuit current (I*sc*) of tap water were 39.2 V and 2.25 mA/m^2 due to the presence of mineral impurities in tap water. Although they achieved high V_{oc} and I*sc* from tap water, the polypropylene (PP) tank was very big, and the process is tedious[25]. The development of evaluation techniques is still needed for the accomplishment of higher TENG efficiency.

Higher hydrophobic rough surfaces are performed a pivotal role to generate instantaneous voltage, and currents when they interact with the water stream and splitting of water through a fast slip down process[26]. Similarly, in the present research work, we developed a simple, economically viable, and eco-friendly higher hydrophobic surface based on a PTFE membrane for a flexible tubing nanogenerator. The PTFE membrane was inserted inside of the flexible tube along with a copper electrode, and connected with a wire. The PTFE surface can work as a fluid TENG when Tap water (TW), and DI water have interacted abruptly and as continuous flow circulation. For simple acronyms and convenience, we named TW-Sh-PTFE-TENG as TW-Sh-TENG, TW-N-PTFE-TENG as TW-N-TENG, DI-Sh-PTFE-TENG as DI-Sh-TENG, and DI-N-PTFE-TENG as DI-N-TENG. The TW and DIw were used for the TW-N-TENG, and DIw-Sh-TENG, which are negatively charged according to the triboelectric series and are easily accessible as non-toxic and non-corrosive. TW-Sh-TENG was selected for the solid support due to its hydrophobicity, high negativity in the triboelectric series including chemical and thermal stability[27–30].

Results

Structure design, and fabrication. The N-/Sh-TENG were fabricated by adhering the N-PTFE/Sh-PTFE films on the aluminum (Al) surface and then fixing it inside a flexible silicone tube (0.5 cm × 15 cm), which was named the N-/Sh-TENG cell. When a stream of Tap Water (TW) or DI water (DIw) was circulated through the N-/Sh-TENG inside of silicone tubing, the protected N-/Sh-TENG cell was received negative ions (electrons) from the TW or DIw streams and generate power due to the presence of N-PTFE/Sh-PTFE film. Subsequently, the water droplets were transformed into a positively charged electric double layer during circulation of the water stream[31].

The water circulation system includes a long silicone pipe that was connected to a water tank as a reservoir (a), a circulation pump with a variable speed drive (b), and PTFE-TENG cell. As soon as the TW droplets were touched the PTFE membrane, a charge imbalance ascends between them. Consequently, when the droplet completely departures the cell, the electrons were transferred from the ground to the Al electrode through an external load, which generates electricity (d). The rectifier circuit (f) is used as an electrical coupling between the PTFE-TENG, and LED (g), as shown in Fig. 1.

Fabrication of PTFE-TENG, and contact angle (CA) studies. A lotus-leaf-like Sh-PTFE film was prepared from N-PTFE film by spraying an acrylic thinner to create the super-hydrophobicity. The acrylic thinner was sprayed on N-PTFE and dried, this process was repeated to generate higher roughness through layer-by-layer deposition to generate super-hydrophobic N-PTFE film such as Sh-PTFE[32]. To determine the wetting performance of the as-prepared Sh-PTFE film, the water contact angle (CA), and water adhesion properties were studied, as shown in Fig. 2. The as-prepared Sh-PTFE showed excellent water repellency (CA = 135°) over the N-PTFE (CA = 96°, Fig. 2a, c). The water droplet (~0.48 µl) is spherical on the modified Sh-PTFE surface (Fig. 2b, d) due to the generation of higher surface roughness like lotus leaf[33,34].

FE-SEM, AFM of N-PTFE, and Sh-PTFE. The surface morphology of N-PTFE, and Sh-PTFE was determined by FE-SEM and AFM analyses, as shown in Fig. 3. A clean surface was found on the N-PTFE (Fig. 3a, b) and whereas on the Sh-PTFE showed micro-corrugated structures (Fig. 3d, e) due to the deposition of acrylic thinner by LBL depositions. Representative micro-corrugate channels were consistently spread on the N-PTFE surface and generated the super-hydrophobic Sh-PTFE[26] which is the key functional material for generation power when interact with flow water. Besides, Fig. 3c, f were showed the Atomic Force Microscopy (AFM) images of N-PTFE(~ 45 nm), and Sh-PTFE(~ 113 nm) and which have been revealed the surface morphologies, and topographical orientations that can represent the L-B-L deposition of acrylic PMMA thinner on the Sh-PTFE surface. The higher surface roughness of Sh-PTFE was displayed superior V_{oc} and I_{sc} than N-PTFE because of the fast sliding nature when interacted with the water on Sh-PTFE. The FT-IR, XRD, and EDX analyses of N-PTFE and Sh-PTFE are discussed in the supporting information[27].

FT-IR, XRD, contact angle, and EDX (Energy dispersive X-ray spectroscopy) of N-PTFE, and Sh-PTFE films. *FT-IR.* The FT-IR analysis showed the evidence of the modification of the Sh-PTFE from N-PTFE, as shown in Fig. 4a. Sh-PTFE showed new absorption peaks at 1407 cm^{-1}, 1450 cm^{-1}, 1732 cm^{-1}, 2805 cm^{-1}, 2905 cm^{-1}, and 2965 cm^{-1} belong to C–(O)–F, CF, CH_2, C=C, and –OH functional groups, respectively, due to formation of carboxylic acid on the Sh-PTFE surface after interaction of TW[23,24]. These peaks were

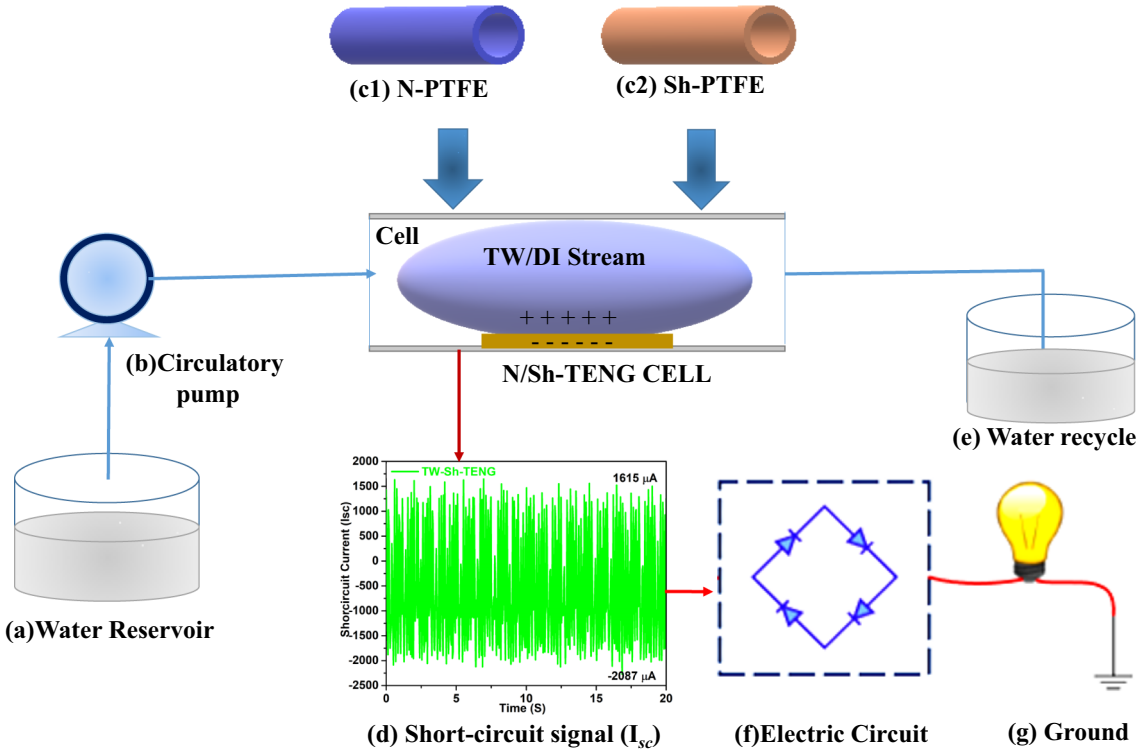

Figure 1. Schematic representation of the Sh-TENG, and N-TENG apparatus.

strongly suggested that the N-PTFE was carbonized by the reaction of acrylic PMMA thinner, and made the Sh-PTFE as a super-hydrophobic rough surface.

XRD. The XRD results were obtained from the diffraction pattern, as shown in Fig. 4b. The N-PTFE exhibited typical crystalline peaks at 15.4°, 18.4°, 31.5°, 36.5°, 44.4°, and 78.2°, which are in agreement with the literature model[24]. The peak intensities for the Sh-PTFE were distorted due to the deposition of acrylic polymer thinner and changed the crystalline pattern. Except for these signals, the N-PTFE and Sh-PTFE patterns look similar and indicate the absence of any obvious crystallinity changes after the interaction with acrylic thinner[35,36].

Contact angles (CA). In order to prepare the substrates for surface modification using commercial PMMA acrylic thinner (Rust-Oleum).The PMMA hydrophobic thinner was deposited by spray coating and drying process and repeated to several time to achieved the desired thickness with layered nano pattern. For that, we used N-PTFE (CA 90.2°), for the deposition surface, as shown in Fig. 4c. After deposition, the surface was exhibited a dramatic increase in CA by sessile drop method, Sh-PTFE exhibiting super hydrophobicity, having CA 135.2° with water droplet, as shown in Fig. 4f. The detailed fabrication process was depicted in Supporting Information, SI-2.

EDX. Energy-dispersive X-ray (EDX) spectroscopy analyses revealed that super hydrophobicity that was achieved by the chemical deposition of acrylic thinner on the Sh-PTFE, as shown in Fig. 4g from N-PTFE Fig. 4d. The atomic %, and weight % of F intensity was decreased from 81.37% (Fig. 4e) to 66.9% (Fig. 4h).with acrylic thinner deposition by chemical reaction, whereas the atomic %, and weight % of C, and O increased from 18.63 to 31.27%, and 0 to 1.83%, respectively. The significant changes in the surface morphologies were achieved by acrylic thinner due to the increase in the oxygen-containing functional groups such as –OH, and –$COOCH_3$ due to the interaction of CF_2 groups of N-PTFE, Fig. 4e. The SEM images of N-PTFE, and Sh-PTFE were suggested the super-hydrophobicity[37–40]. Significant morphological changes were observed on the Sh-PTFE rather than the N-PTFE surface, as shown in Fig. 4h, which indicated that oxygen atoms were existing on the Sh-PTFE surface.

Discussion. *Mechanism of the chemical-reaction pathway between the water N-TENG and Sh-TENG, and their FT-IR, and XRD analyses.* Mechanism. The output voltage, and currents of flow TENG were generated from the strong interaction of TW water with Sh-TENG during TW water circulation, where the water can split into hydronium (H^+), and hydroxide ions (OH^-). To observe the dynamic interactions between CF_2 of Sh-PTEFE and water at atomic level interactions were noted, as shown in Fig. 5a[41]. In particular, the OH– ions were replaced methoxy ions (–OCH_3) by the nucleophilic substitution and elimination mechanism at the PMMA spacer, and made into terminal carboxylic acids. Subsequently, the dissolved metal ions in TW were temporarily

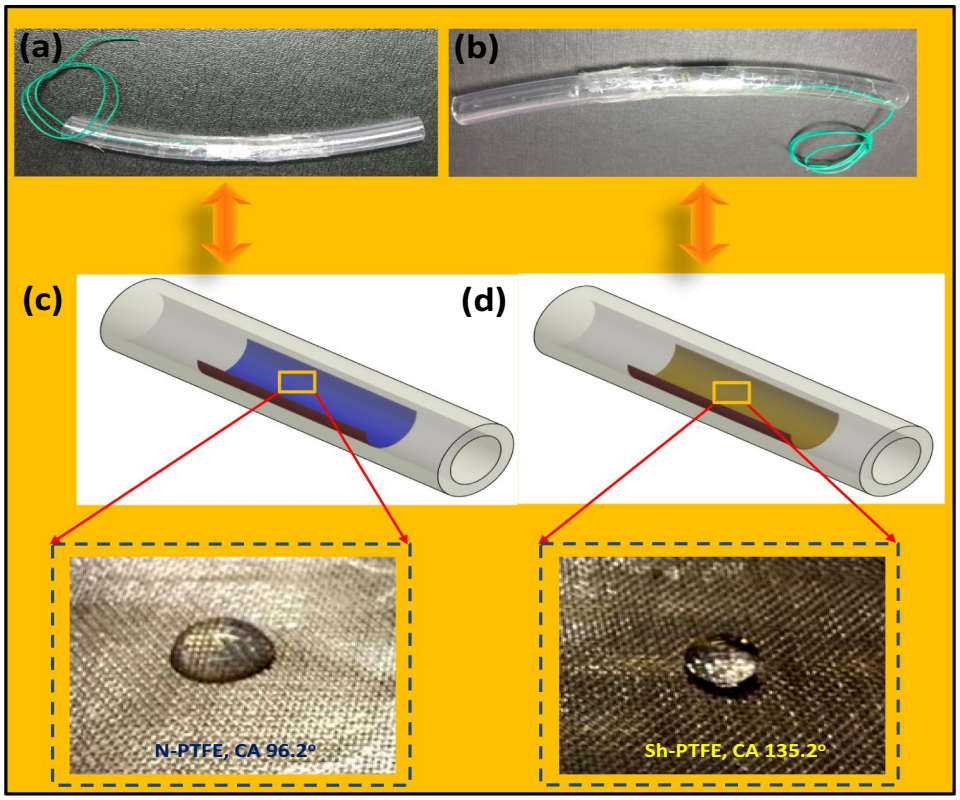

Figure 2. Digital photos of large droplets (~ 5 µl) placed on (**a**) N-TENG cell, (**b**) Sh-TENG cell, (**c**) N-PTFE (CA = 96°), (**d**) Sh-PTFE (CA = 135.2°).

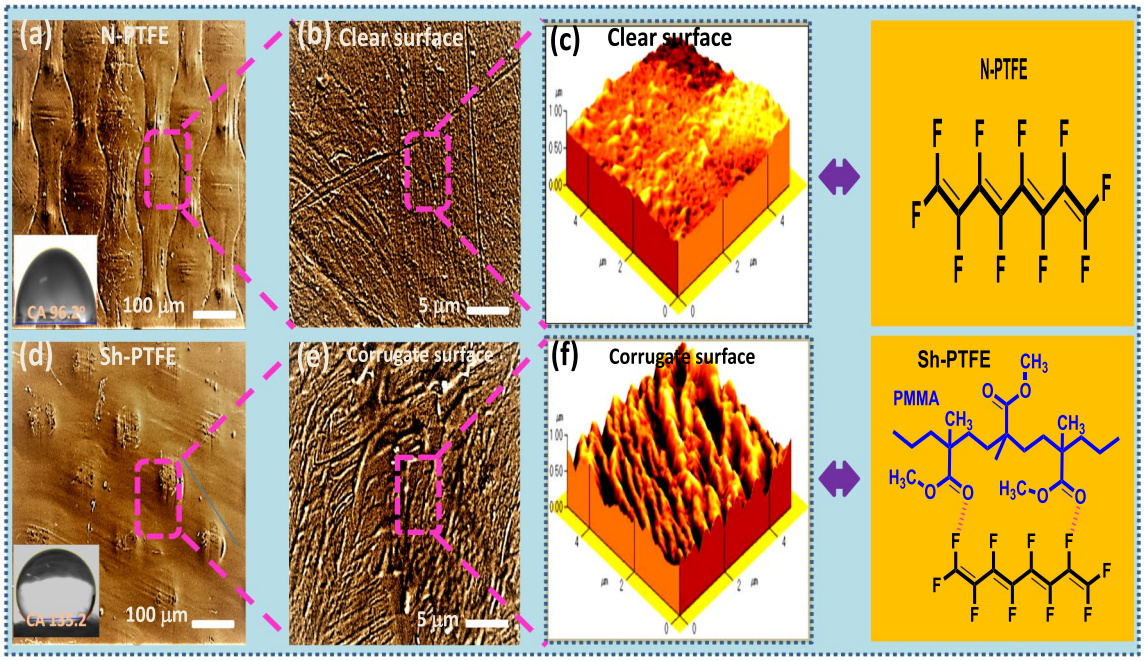

Figure 3. The SEM images showed (**a**, **b**) clean surface of N-PTFE(inset: CA of 96.2°), and (**d**, **e**) corrugated surface of Sh-PTFE, (inset: CA of 135.2°). The AFM images revealed (**c**) clear surface morphology on N-PTFE film (the height of the layer ~ 45 nm) (**f**) and corrugate morphology on Sh-PTFE film (the height of the layer ~ 113 nm).

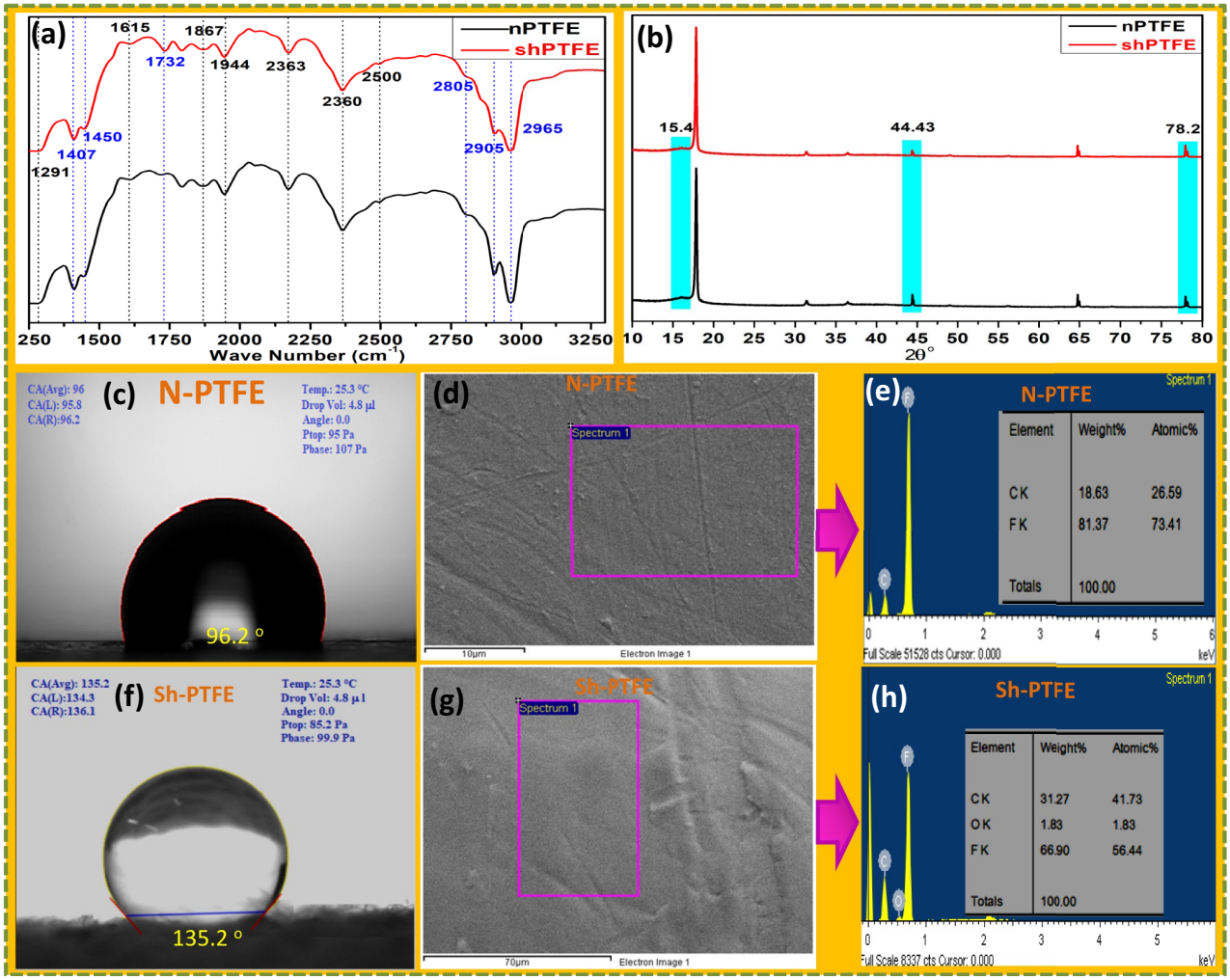

Figure 4. (**a**) FT-IR, (**b**) XRD, (**c**, **f**) CAs, and, (**d**, **g**) SEM-EDX, (**e**, **h**) elemental analysis of both N-PTFE and Sh-PTFE surfaces.

chelated with -COOH groups, and produced metal salts –COOM (i.e. M = H^+, Na^+, Mg^{2+}, and Ca^{2+}). Next, the quantum chemical molecular dynamics (QCMD) were investigated by Onodera et al. to identify the formation of carbonyl functional groups on the back bone chain of PTFE, and water was the counter fluid during the tribo-chemical reaction[34]. Besides, Pletincx et al. have reported the -COOH groups have obtained after the interaction of water molecules with a PMMA surface, and elimination of CH_3OH as a by-product. Thus, the FT-IR analysis of our Sh-PTFE is well judged with their reported information[42].

Figure 5b shows the FT-IR spectra of N-PTFE, TW-Sh-TENG, and DI-Sh-TENG were revealed splitting and generation of H^+ ions on the Sh-PTFE surface. The generated H^+ ions are responsible to produce V_{oc} and I_{sc} through a charge transfer mechanism during the interaction of TW with the Sh-PTFE surface, as shown in Fig. 6a. From the N-PTFE, two strong bands occurred near 1157 cm^{-1} and 1218 cm^{-1}, which correspond to the main $–CF_2$ chains of the symmetric and anti-symmetric stretching bands of v(C–C) vibration manifests in the form of modulation at 1258 cm^{-1}[43–45].

After the interaction of TW with the Sh-PTFE surface, the intensity of anti-symmetric stretching bands of the CF_2 was reduced due to the interactions between the H^+ ions in water. Consequently, the new stretching bands have appeared at 1551 cm^{-1}, 1611 cm^{-1}, 1736 cm^{-1}, 2177 cm^{-1}, 2363 cm^{-1}, 2807 cm^{-1}, 2851 cm^{-1}, 2962 cm^{-1}, and 3376 cm^{-1}, which were corresponding to PMMA-COOH, and –OH functional groups owing to the formation of $C^+–F^–H^+$ transition bonds, respectively. In the case of PTFE-COOH, a medium band appeared at 1551 cm^{-1}, which belongs to C=C of PTFE, which was interacted with water, and form a –C–(OH)–C– bond. A band appeared at 1736 cm^{-1} of Sh-TENG because of the absorption by the –CO– of COOH. Besides, a strong broad absorption band appears at 3309 cm^{-1}, which represents the presence of –CF=C–COOH, and revealed the formation of PMMA-COOH after hydrolysis of PMMA methyl ester, as explained in Mechanism-2[44]. As a result, the mechanistic approach is strongly suggested by the interaction of the FT-IR spectrum was strongly suggested a mechanistic approach for the Sh-TENG, and N-TENG interaction with TW, and DIw[25,41,45,46].

After fluid TENG experiments, the dissolved salts in TW such as (M = H^+, Na^+, Mg^{2+}, and Ca^{2+}) and DI were deposited on the surface of N-PTFE and Sh-PTFE and quantified the degree of crystallinity by the XRD analysis,

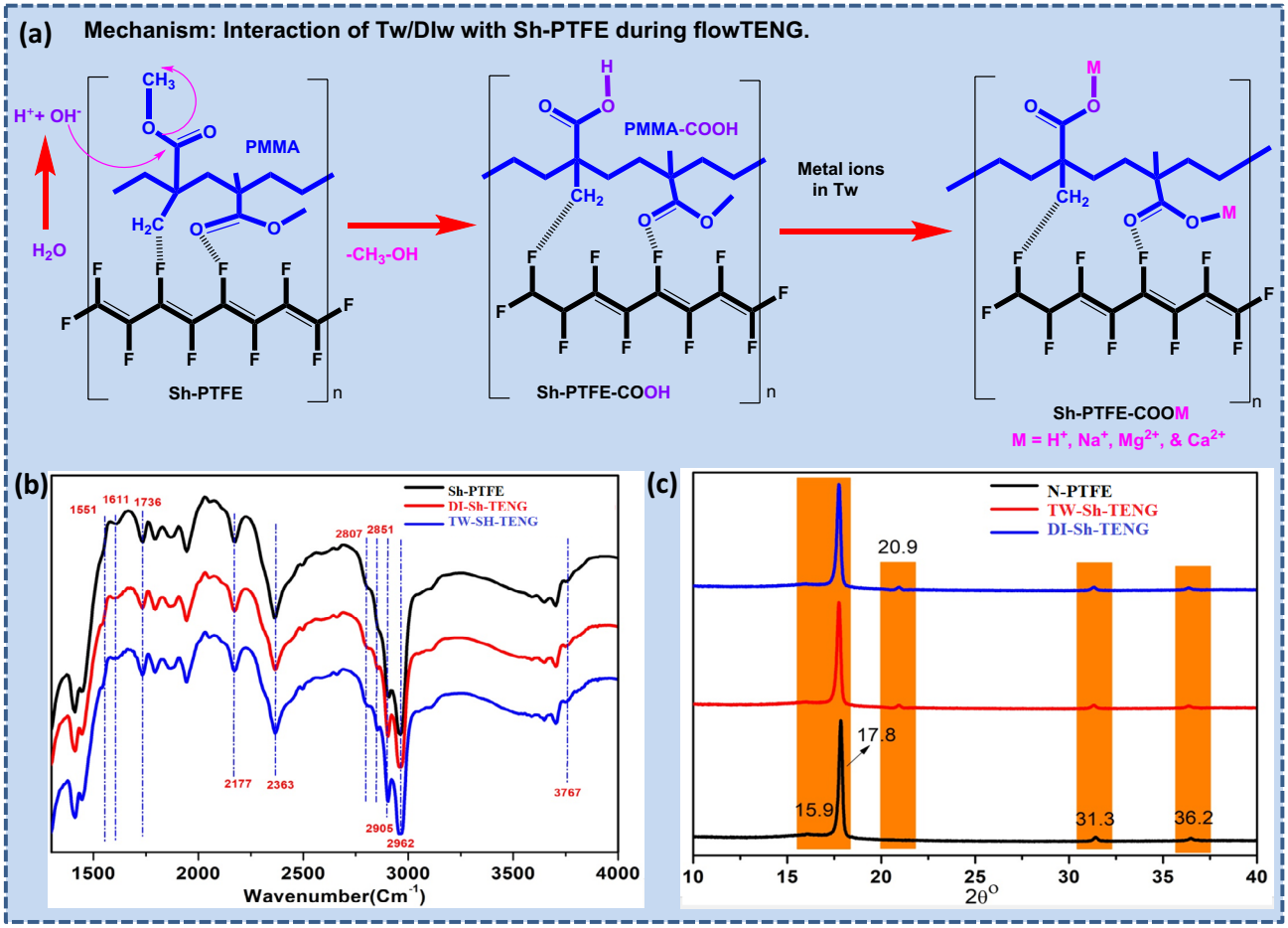

Figure 5. Schematic representation of mechanism of (**a**) Sh-PTFE with water molecules and nucleophilic elimination of CH_3OH; (**b**) FT-IR; and (**c**) XRD spectra of N-PTFE and Sh-PTFE.

as shown in Fig. 5c. The N-PTFE exhibited typical XRD peaks at 15.9°, 17.8°, 31.3°, and 36.2°, which are in agreement with the literature[23]. The new peak was observed at 20.9°, and also, peak intensities were reduced from Tw-Sh-TENG to DI-Sh-TENGs due to the formation of -COOH groups on the Sh-PTFE surface[35].

Mechanical pathway for the characteristic discontinuous current generation. Figure 6 showed the performance of the flow TENG using various TW-Sh-TENG, TW-N-TENG, DI-Sh-TENG, and DI-N-TENGs. To generate the pulsatile stream, a three-roller peristaltic drive (Ecoline VC-360) was used in this research, Fig. 6a. The long go through silicon tubing with the N-PTFE/Sh-PTFE-TENG cells as described in the material section and which were used for the fluid passage which is constantly flowing the working fluid, Fig. 6b. To quantify the charge generation mechanism in the N-PTFE/Sh-PTFE-TENG cells from the fluid stream, which is compared with the Chapman-Stern layer mathematical model that was combined the hydrodynamics and electrostatic stimulation in the PTFE-TENG solid–liquid interface was elucidated with the aid of electrical double layer formation[47]. When the flowing liquid starts rolling on the silicon tubing, the Si–O–H were momentarily protonated and accommodates the opposite counter ions of the flowing liquid at the solid–liquid boundary. Owing to the rigid (no-slip, $U = 0$) border ailment at the barrier, the extremely intense ions were immobile within the solid–liquid interface through the working fluid flows, Fig. 6c. The hydrophobic properties of the N-PTFE/Sh-PTFE surfaces provide slip condition ($U \neq 0$) at the solid–liquid interface facilitates extremely focused ions to be moveable in the range of slip-up plane, and hard border and then enhances the liquid flow velocity[48,49]. The ions were at the slip plane that maintains remain the similar velocity along with liquid flow above the N-PTFE/Sh-PTFE surfaces. After the interaction of the flow working fluids, the generated V*oc* and I*sc* were quantified using Techtronics digital oscilloscope, Fig. 6d (Supplementary information 1 and 2).

Results of N-TENG, and Sh-TENG through a 3 roller peristaltic circulation pump. The liquid used for the flow TENGs is water-based and is positively charged according to the triboelectric series. The liquid is easily accessible, non-toxic, and non-corrosive. N-PTFE was chosen on the solid side owing to its hydrophobicity with high negativity in the triboelectric series, and chemical constancy[26]. To develop N-TENG (Fig. 2a), and Sh-TENG (Fig. 2b), we placed normal PTFE (N-PTFE) (Fig. 2c), or super-hydrophobic PTFE (Sh-PTFE) (Fig. 2d) films with a thickness of 0.08 mm on general-purpose aluminum tape. The flow TENG was fabricated

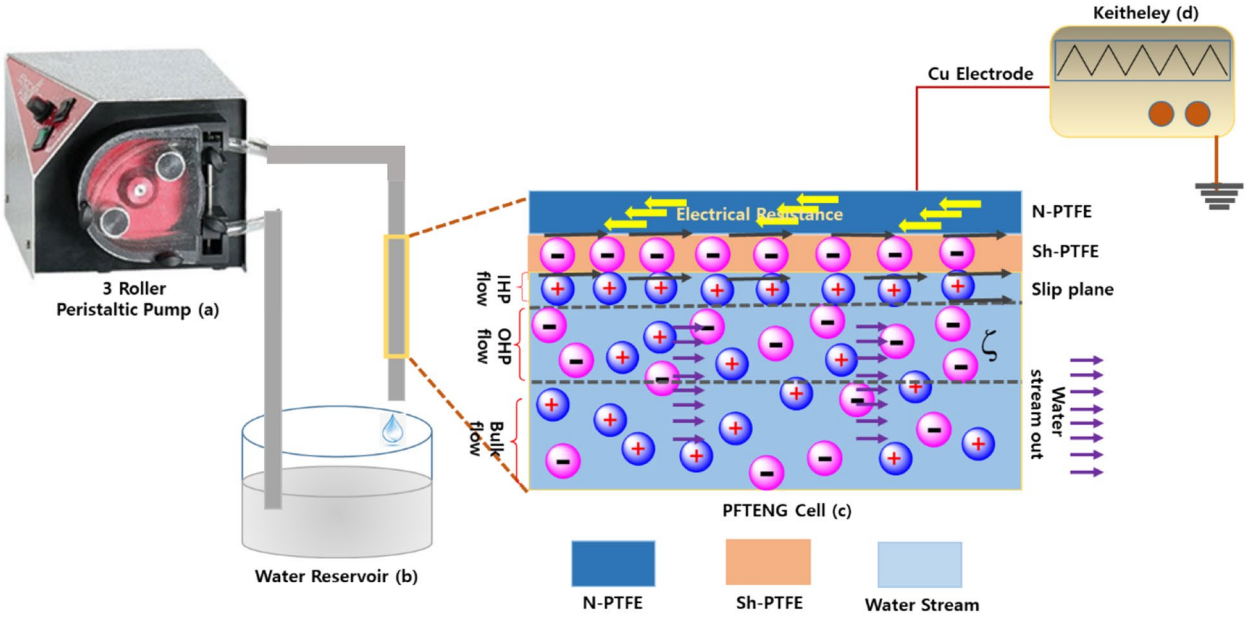

Figure 6. Mechanistic approach to generate the Electric double layer (EDL) for power supply through (**a**) peristaltic pump, (**b**) water reservoir (**c**) TENG cell showing the EDL = IHP + OHP at the interface of solid–liquid and the reduction of the zeta potential after the IHP to the bulk segment of the flow liquid. (**d**) Electrometer. (Supporting information showed the picture of live experimental set-up of for the proposed flow TENG Apparatus).

by adhering the N-PTFE/Sh-PTFE layer to an aluminum (Al) surface and then fixed inside a general-use flexible silicone tube (0.5 cm × 15 cm). The Sh-PTFE was obtained by deposition of acrylic PMMA Previously, we described upon the contact the liquid with PVDF membrane and generated power output through peristaltic pump[50], similarly, the present work of N-PTFE/Sh-PTFE surfaces, due to its CH_3 groups were transformed into highly electronegative of CH_2– so thus attracting the positive counter ions following the electrostatic induction and triboelectrification. This phenomenon motives the development of an Electric Double Layer (EDL) within the sliding plane. The EDL contains Inner Helmholtz Plane (IHP) where the positive counter ions can move peripherally along with the flow direction over the N-PTFE/Sh-PTFE surfaces, and the other one Outer Helmholtz Plane (OHP) whereas the mobile positive ions and the counter ions can transpire together, as shown in Fig. 6. In the IHP, the drive of the counter ions was strongly influenced by the common hydrodynamic liquid stream in the pipe flow. The counter ions can move superficially alongside the slide range of the boundary partition but showed uncertainty to be gathered in the OHP or in the bulk liquid. In the case of OHP, the reverse polarized could travel to the bulk liquid. For instance, the flowing liquid was viscid, and incompressible by the Newtonian liquid, then peristaltic flow at the PF-TENG cell-liquid interface, the continuity and Navier Stokes equations clench worthy and can be modified for the ion's drive in the IHP[51,52].

$$\frac{\partial \rho}{\partial t} = \nabla \cdot (\rho v_{fluid}) = 0 \tag{1}$$

where ρ and υ_{fluid} remain the density, and velocity of the working fluid, correspondingly.

The modified Navier–Stokes equation

$$\rho \frac{\partial v_{fluid}}{\partial t} + \rho (v_{fluid} \cdot \nabla) v_{fluid} = \nabla \cdot [-\rho I + \mu (\nabla v_{fluid} + (\nabla v_{fluid})^T)] + F_n \tag{2}$$

where F_n was the body force vector forced on the liquid. In our system, the body force was the applied electrostatic magnetism power in usual direction between the surface electrons of the PTFE surface, and the positive charges in the IHP. Allowing to the Guoy–Chapman theory[53], this magnetism power could be in the rolling form

$$F_n = \frac{(qE_n = A_p \sigma^2)}{(\varepsilon_0 \varepsilon_1)} \tag{3}$$

Here, q is the electrical charge, A_p is the effective contact area, σ is the surface charge density, ε_0 and ε_1 are the dielectric permittivity of the vacuum, and working liquid. Where at the PTFE liquid interface, the liquid was positively charged owing to high dielectric constant rendering to Cohen's rule[54].

$$\rho = 1.5 \times 10^{-5} (\varepsilon_1 - \varepsilon_2) \tag{4}$$

Here, ε_2, ρ are the dielectric constant of the Sh-PTFE, and the space charge density, correspondingly. The Debye characteristic length at the IHP was expressed by,

$$\lambda_D = \frac{\xi \varepsilon_0 \varepsilon_1}{\sigma} \tag{5}$$

where ξ was the Zeta potential as represented in Fig. 6c, it is gradually decreased from IHP to working liquid. The shear stress τw of the liquid was enacted on the wall can be written by Ref.[55].

$$\tau_w = \frac{2\mu v_i}{R = \lambda_D} \tag{6}$$

In Eq. (6), the υi was the ion velocity that is equal to the υ fluid at the IHP, and the circle of the flow tube R was substituted by the Debye Length. So, the implicit shear force, and the derived ion velocity was expressed by Eqs. (7) and (8), correspondingly.

$$F_s = A_p \tau_w = A_p \mu \frac{2v_i}{\lambda_D} \tag{7}$$

$$v_i = \frac{\tau_w \lambda_D}{2\mu} \tag{8}$$

Due to the slide boundary condition when applied on the over the PTFE surface the ions velocity υi was multiplied by the factor of (1 + bλD)[56], where b was the slip length. So, the ion velocity becomes

$$v_i = \frac{\tau_w \lambda_D^2}{2\mu(\lambda_D + b)} \tag{9}$$

The static rubbing force in the solid PTFE surface that was reacted oppositely to the shear force was equal to the F_n, and multiplied with the friction coefficient μ_s subsequently followed by the Amonton's law of stationary resistance

$$F_f = \mu_s F_n \tag{10}$$

The ions were started to slip against the solid border of the film once Fs > Ff. Alternatively, on the solid surface the electrons were pulled by the sheer force of the ions, but the velocity was delayed due to the electrical resistance of the solid. During this time, the momenta was preserved for both the counter ions, and electrons at the interface. The electrons were pulled back by the ions affecting comparative distance thus velocity difference was induced the potential difference in the interface, and short circuit current by the external load. The Drude model is adopted by the solid-state physics showed electrons on the solid surface

$$\frac{d(mv_e)}{dt} = \frac{-mv_e}{\tau + qE_{ext}} \tag{11}$$

where υ_e, τ, ${}_qE_{ext}$ were velocity of electrons, Drude relaxation time, and applied outside arena. In this model, the electrostatic attraction was strong enough that the electrons were dragged by the quicker ions in the IHP. As the external applied was zero, so Eq. (10) reduces to

$$\frac{d(mv_e)}{dt} = \frac{-mv_e}{\tau} \tag{12}$$

The momenta are preserved by the electrons across the interface,

$$\frac{F_s + d(mv_e)}{dt} = 0 \tag{13}$$

Combining both Eqs. of (10), and (11) the electron velocity becomes as follows

$$v_e = \frac{F_s \tau}{m} \tag{14}$$

Now, the net amount of induced charges in the Sh-PTFE surface owing the electrostatic potential triggered by the comparative distance between the electrons, and flow ions,

$$Q_s = \sigma_0 S = \sigma_0 wx \tag{15}$$

The prompted net electric power in the solid surface is provided by

$$I_s = \frac{dQ}{dt} = \sigma_0 w \frac{dx}{dt} = \sigma_0 w \Delta v = \sigma_0 \pi a (v_i - v_e) \tag{16}$$

The resultant PTFE surface electric potential owing to the electrical resistance, R, and electric power is

$$\psi_s = I_s R = \frac{I_s}{bK_s} \tag{17}$$

where b is the distance of the ${}_qE_{ext}$ and K_s is the surface conductivity.

Based on the resulting Eqs. (9), (14), and (17) for the ions velocity, electrons velocity, and surface potential of the PTFE surfaces, correspondingly, the triboelectrification owing to the pulsatile flow over the PTFE surfaces can be explained.

Results of flow-TENG. Also, the contact electrification in metal-dielectric cases was strongly studied by Z. L. Wang et al. where they have elaborated various metal-dielectric cased to generate the power output through a contact-electrification process[57]. The present studies revealed that the electrical outputs of the proposed Flow-TENG surfaces are demonstrated in this section. All measurements refer to an operating speed of 350 rpm/min, which can be manually controlled by the tubing pump (Ecoline VC-360). The Flow-TENG was produced instantaneous peak-to-peak values of open-circuit voltages (Voc), and short-circuit currents (Isc) and compared with different unmodified and modified surfaces such as N-PTFE and Sh-PTFE, respectively. For simple acronyms and convenience, we named TW-Sh-PTFE-TENG as TW-Sh-TENG, TW-N- PTFE-TENG as TW-N-TENG, DI-Sh-PTFE-TENG as DI-Sh-TENG, and DI-N-PTFE-TENG as DI-N-TENG. It is observed that the V*oc* and I*sc* of Flow-TENGs, TW-Sh-TENG, TW-N-TENG, DI-Sh-TENG, and DI-N-TENG were produced of 29.3 V (Fig. 7a), 17.4 V (Fig. 7b), 15.9 V (Fig. 7c), and 12.4 V, (Fig. 7d). Next, the I*sc's* were obtained 3.7 μA (Fig. 8a), 2.9 μA (Fig. 8b), 2.7 μA (Fig. 8c), and 1.8 μA (Fig. 8d), from TW-Sh-TENG, TW-N-TENG, DI-Sh-TENG, and DI-N-TENG, respectively. The attributed values were suggested that the V*oc* of TW-Sh-TENG was showed 139% higher than that of V*oc* of DI-Sh-TENG, and the I*sc* of TW-Sh-TENG is 101% than DI-N-TENG, respectively, due to the lack of dissolved ions in DI water, also, sufficient roughness, and super-hydrophobicity on the N-PTFE surface. The constant Voc and Isc were observed in all pulsatile streams for one to five cycles which are represented in inset images, as shown in Figs. 7 and 8. Besides, the mechanistic explanation was strongly suggested the TW-Sh-TENG was shown superior V*oc,* and I*sc* over DI-Sh-TENG because of higher dissolved mineral salts in TW that can further enhance the generation of higher power output compared to DIw-TENG[57–59].

Power output studies. Subsequently, the performance under different external loads was investigated. The maximum power output was achieved by TW-Sh-TENG using TW using various load resistances of 1 MΩ to 23.44 MΩ. The dependence of the power output curves and power density as functions of the resistance are shown in Fig. 9. When increasing the load resistance, the power output increased up to a maximum value and then decreased. The power reached its maximum value at an external load resistance of 11.72 MΩ (green vertical lines). The maximum powers were obtained at 11.72 MΩ for 76.9 μW (TW-Sh-TENG), 27.4 μW (TW-N-TENG), 18.5 μW (DI-Sh-TENG), and 14.3 μW (DI-N-TENG, respectively, as shown in Fig. 9a. On the other hand, the maximum power densities were obtained at 11.69 MΩ for 38.2 μW/cm^2 (TW-Sh-TENG), 13.8 μW/cm^2 (TW-N-TENG), 9.6 μW/cm^2 (DI-Sh-TENG), and 7.1 μW/cm^2 (DI-N-TENG), respectively, as shown in Fig. 9b[57–59]. The TW-Sh-TENG produced significantly higher power output over normal TW-N-TENG (178%), which verified the importance of super-hydrophobicity in water-based TENGs[60,61].

Next, the peak-to-peak open-circuit voltages were 29.4 V for TW-Sh-TENG, 17.4 V for TW-Sh-TENG, 15.7 V for DI-Sh-TENG, and 12.3 V for DI-N-TENG, respectively, as shown in Fig. 9c. The short-circuit currents were 3.7 μA for TW-Sh-TENG, 2.9 μA for TW-Sh-TENG, 17.4 V for TW-Sh-TENG, 2.7 μA for DI-Sh-TENG, and 1.8 μA for DI-N-TENG, respectively, as shown in Fig. 9d. The Voc and Isc have suffered a predictable drop in magnitude from TW-Sh-TENG to DI-N-TENGs, as shown in Fig. 9c, d. The output power of DI-N-TENG dramatically decreased by 4 times compared to DI-Sh-TENG from 76.9 to 18.5 μW, and the power density decreased from 38.2 to 9.6 μW/cm^2[62]. The power output of TW from the TW-Sh-TENG is up to 300% higher than that with DI-TENG. Similarly, TW-N-TENG produced a higher power output of 94% with TW compared to DI. In the case of power density, we observed higher values from TW-Sh-TENG than TW-N-TENG and the power densities were 178% and 33%, respectively due to the H^+ ions expelled F- ions as HF from the surface[56,63]. More importantly, TW contains dissolved mineral salts that can enhance the power output compared to DI water. Besides, the performance stability of the designed TW-Sh-TENG has been tested for 12,000 cycles and received the constant voltage, as shown in Fig. 9e. The test results strongly supported our idea for using the TW-Sh-TENG has been produced superior Voc and Isc compared with other designated flow TENGs due to the higher irregular surface morphology, and super-hydrophobicity[64,65].

Methods

Material descriptions. The liquid was used for the flow TENGs is water-based and is positively charged according to the triboelectric series. The liquid is easily accessible, non-toxic, and non-corrosive. N-PTFE was selected for the solid surface owing to its hydrophobicity, higher negativity in the triboelectric series, and chemical stability[26]. To develop N-TENG (Fig. 2a), and Sh-TENG (Fig. 2b), we placed normal PTFE (N-PTFE) (Fig. 2c), or super-hydrophobic PTFE (Sh-PTFE) (Fig. 2d) films with a thickness of 0.08 mm on general-purpose aluminum tape. The flow TENG was fabricated by adhering the N-PTFE/Sh-PTFE layer to an aluminum (Al) surface and then fixed inside a general-use flexible silicone tube (0.5 cm × 15 cm). The Sh-PTFE was obtained by deposition of acrylic PMMA thinner (Rust-Oleum Corporation, USA).

To characterize the surface properties, the contact angle (θ) was used. The contact angle of DI water on the Sh-PTFE surface was conducted with a DSA 100 Goniometer (error ± 1°) using the sessile-drop method (droplet volume: 0.48 μl) (KRUSSG mbh, Hamburg, Germany). The sample surface morphology was determined by a Hitachi cold FE-SEM microscope working at 10 kV. 2.2. The functional groups were measured by a Nicolet 6700

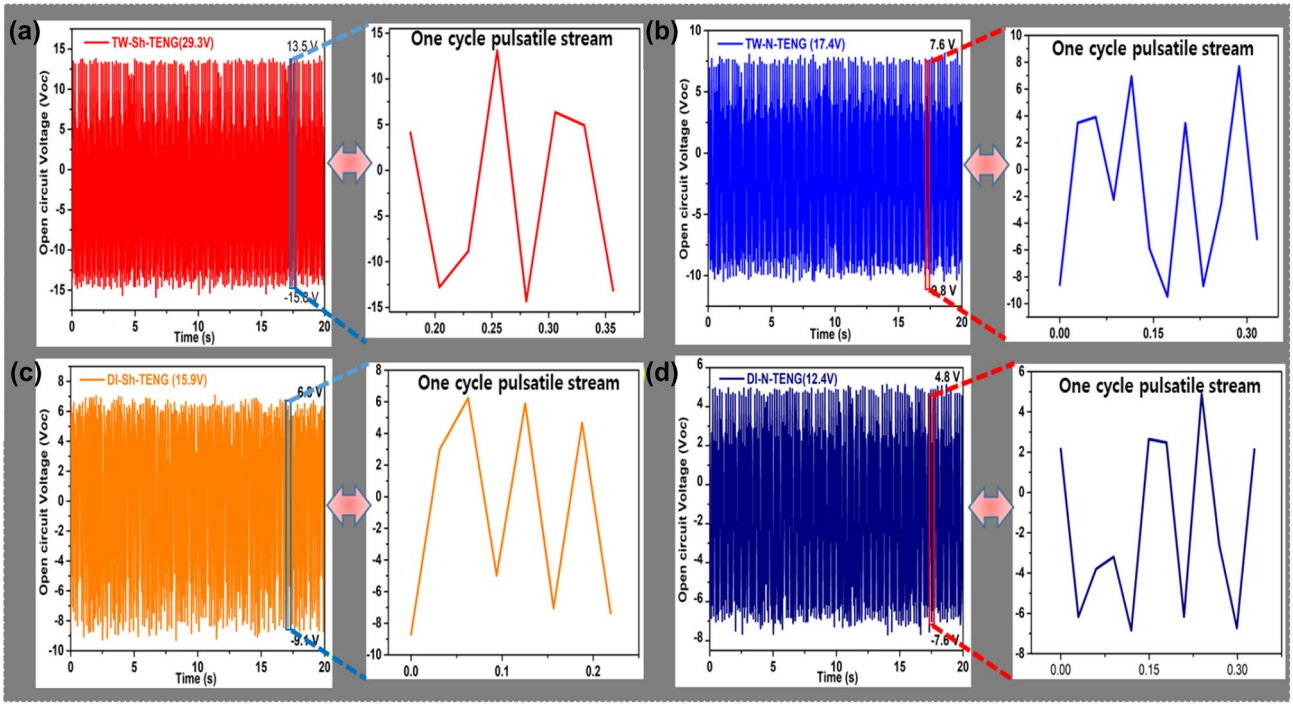

Figure 7. The open-circuit voltages (V_{oc}) of (**a**) TW-Sh-TENG; (**b**) TW-N-TENG; (**c**) DI-Sh-TENG; (**d**) DI-N-TENG and their single to three pulsatile open-circuit voltages (V_{oc}) showed in the inset images.

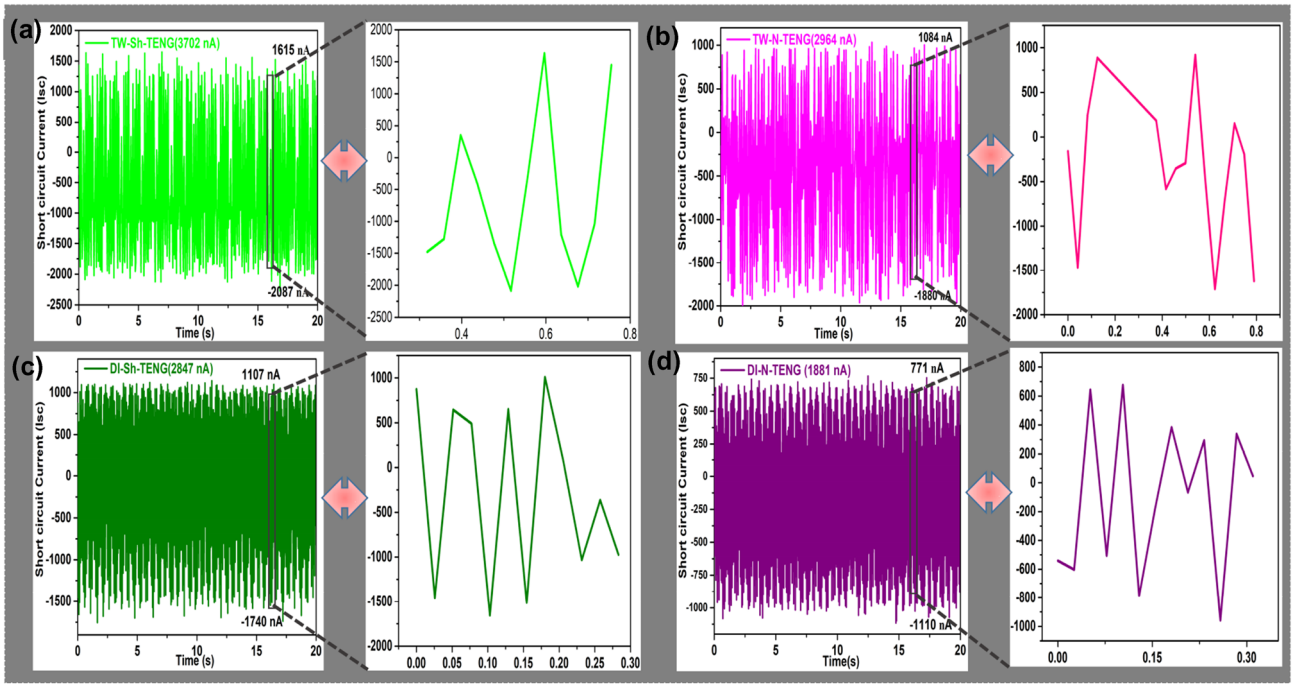

Figure 8. The short-circuit current (I_{sc}) of (**a**) TW-Sh-TENG; (**b**) TW-N-TENG; (**c**) DI-Sh-TENG; (**d**) DI-N-TENG and their single to three pulsatile open-circuit voltages (V_{oc}) showed in the inset images.

FT-IR, Diffraction data were acquired with a Rigaku high-power XRD. The images of the Multimode V AFM microscope (VEECO, US) were treated using a flattening algorithm in Nanoscope software, and the surface roughness average (Ra) was calculated using the instrument vendor's software.

A simple electric circuit was designed to evaluate the load features, and harvest performance of the liquid nanogenerator through flow TENGs. The circuit that includes with a full bridge rectifier, a capacitor for

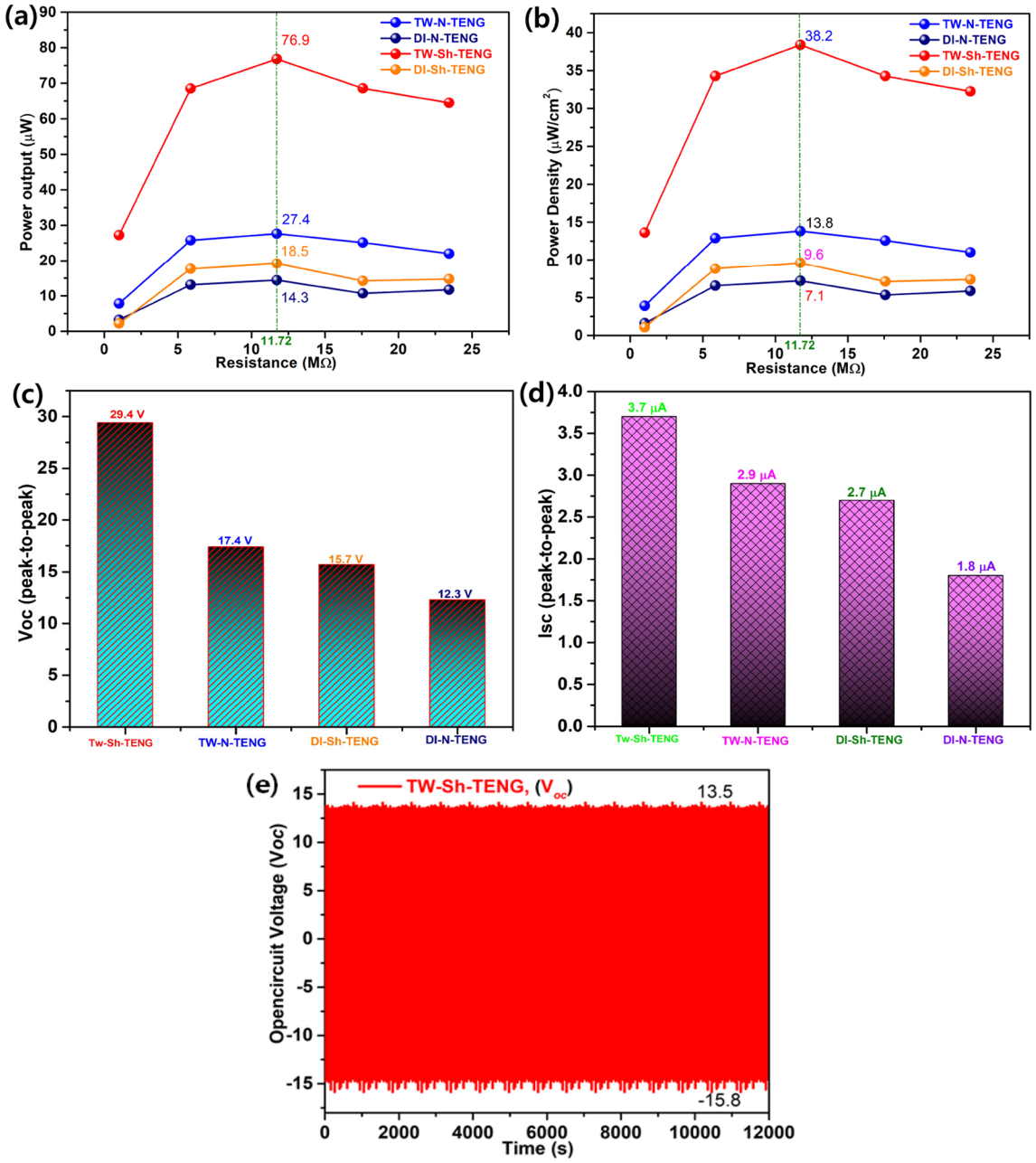

Figure 9. The power output (**a**); power density (**b**) and comparison of overall V_{oc} (**c**) and I_{sc} (**d**) of TW-Sh-TENG, TW-N-PTFE-TENG, DI-Sh-TENG and DI-N-TENG; (**e**) stability and durability test for 12,000 s were also conducted to confirm the durability and sustainability.

energy storage to correct the cycled positive and negative signals, and store the transformed electricity. Tektronix TBS1102B Digital Oscilloscope was used to analyze the generated Voc and Isc[66–68].

Surface modification and characterization. The surface hydrophobicity of the solid tubing plays an important role in the output performance of Sh-TENG because the with-holding of liquid droplets, which could monitor the charges on the solid surface and thus reduce the power output. Since N-PTFE does not have high hydrophobicity, surface modification is necessary to enhance it. The Sh-PTFE was prepared by spraying acrylic thinner in mineral spirits and heated at 50 °C for 30 min (see the supporting information).

Super hydrophobicity and contact angle (CA). Hydrophobicity and super hydrophobicity behaviours of N-PTFE, and Sh-PTFE were examined via the CA measurement technique through a sessile drop of water. It was achieved that as received Sh-PTFE is exhibited super hydrophobic nature from N-PTFE due to increasing roughness on the surface by deposition of PMMA spacer. The PMMA spacer contains methyl ester groups which

can enhance the surface tension to increase the contact angle. In particular, the CAs of N-PTFE and Sh-PTFE were 96° and 135.2°, respectively.

Conclusion

For the first time, we introduced flexible silicone-pipe TENGs based on TW, and DI water. The fabrication of N-PTFE/Sh-PTFE films that were fixed inside the flexible silicone pipe has advantages that include easy handling, cheapness, eco-friendliness, and portability. The proposed Sh-PTFE-TENG is highly durable for circulation of tap water to generate higher V_{oc} and I_{sc}. The Sh-PTFE surface was achieved by a very simple method of spray coating PMMA acrylic thinner. Water plays a pivotal role on the surface of N-PTFE, where nucleophilic substitution occurs at the terminal CF_2 group to form a carboxylic acid group. At the Sh-PTFE surface, the water can hydrolyze the methoxy group, which leads to the formation of methanol and a carboxylic acid functional group. The interaction of water molecules is critical, which was elucidated through the mechanism and experiment and confirmed by FT-IR, and XRD analyses.

The TW-Sh-TENG, and TW-N-TENG were shown V_{oc}, and I_{sc} of 29.4 V, and 3.7 μA and 17.4 V, and 2.9 μA, respectively. The V_{oc} and I_{sc} of DI-Sh-TENG and DI-N-TENG were achieved of 15.7 V, and 2.743 μA and 12.3 V, and 1.836 μA, respectively. The performance under different external loads was investigated, resulting in maximum power of 76.9 μW for TW-Sh-TENG, and 27.6 μW for TW-N-TENG, which correspond to power densities of 38.2 $\mu W/cm^2$, and 13.8 $\mu W/cm^2$ at 11.7 MΩ. The output power and power density dramatically decreased by 4 times from 76.9 to 18.9 μW, and from 38.3 to 9.6 $\mu W/cm^2$ compare to the TW-Sh-TENG with DI-N-TENG. The TW-Sh-TENG produced significantly higher output power over the normal surface (178%), it indicated that it is strongly needed the development of super-hydrophobic surfaces for fast ionic interactions in water-based TENGs.

Received: 12 July 2021; Accepted: 28 December 2021
Published online: 08 March 2022

References

1. Lowell, J. & Rose-Innes, A. C. Contact electrification. *Adv. Phys.* **29**, 947–1023 (1980).
2. Fan, F. R., Tian, Z. Q. & Wang, Z. L. Flexible triboelectric generator. *Nano Energy* **1**, 328–334 (2012).
3. Fan, F. R. *et al.* Transparent triboelectric nanogenerators and self-powered pressure sensors based on micropatterned plastic films. *Nano Lett.* **12**, 3109–3114 (2012).
4. Zhu, G. *et al.* Triboelectric-generator-driven pulse electrodeposition for micropatterning. *Nano Lett.* **12**, 4960–4965 (2012).
5. Wang, S., Lin, L. & Wang, Z. L. Nanoscale triboelectric-effect-enabled energy conversion for sustainably powering portable electronics. *Nano Lett.* **12**, 6339–6346 (2012).
6. Zhu, G. *et al.* Toward large-scale energy harvesting by a nanoparticle-enhanced triboelectric nanogenerator. *Nano Lett.* **13**, 847–853 (2013).
7. Wiles, J. A., Grzybowski, B. A., Winkleman, A. & Whitesides, G. M. Toward large-scale energy harvesting by a nanoparticle-enhanced triboelectric nanogenerator. *Anal. Chem.* **75**, 4859–4867 (2003).
8. Diaz, A. F. & Guay, J. Contact charging of organic materials: Ion vs. electron transfer. *IBM J. Res. Dev.* **37**, 249–260 (1993).
9. Horn, R. G., Smith, D. T. & Grabbe, A. Contact electrification induced by monolayer modification of a surface and relation to acid–base interactions. *Nature* **366**(442–443), 442–443 (1993).
10. Horn, R. G. & Smith, D. T. Contact electrification and adhesion between dissimilar materials. *Science* **256**, 362–364 (1992).
11. Soh, S., Kwok, S. W., Liu, H. & Whitesides, G. M. Contact de-electrification of electrostatically charged polymers. *J. Am. Chem. Soc.* **134**, 20151–20159 (2012).
12. McCarty, L. S., Winkleman, A. & Whitesides, G. M. Ionic electrets: electrostatic charging of surfaces by transferring mobile ions upon contact. *J. Am. Chem. Soc.* **129**, 4075–4088 (2007).
13. Zhao, D., Duan, L. T., Xue, M. Q., Ni, W. & Cao, T. B. Patterning of electrostatic charge on electrets using hot microcontact printing. *Angew. Chem. Int. Ed.* **48**, 6699–6703 (2009).
14. Bandodkar, A. J., Jeerapan, I. & Wang, J. A comparative study on gas sensing performance of photo-reduced GO with TiO2 and ZnO. *ACS Sens.* **1**, 464–482 (2016).
15. Kim, D. *et al.* Triboelectric nanogenerator based on the internal motion of powder with a package structure design. *ACS Nano* **10**, 1017–1024 (2016).
16. Zhu, G. *et al.* Self-powered, ultrasensitive, flexible tactile sensors based on contact electrification. *Nano Lett.* **14**, 3208–3213 (2014).
17. Lin, Z. H., Cheng, G., Wu, W., Pradel, K. C. & Wang, Z. L. Dual-mode triboelectric nanogenerator for harvesting water energy and as a self-powered ethanol nanosensor. *ACS Nano* **8**, 6440–6448 (2014).
18. Tang, W. *et al.* Liquid-metal electrode for high-performance triboelectric nanogenerator at an instantaneous energy conversion efficiency of 70.6%. *Adv. Funct. Mater.* **25**, 3718–3725 (2015).
19. Lin, Z. H., Cheng, G., Lin, L., Lee, S. & Wang, Z. L. Water–solid surface contact electrification and its use for harvesting liquid-wave energy. *Angew. Chem.* **125**, 12777–12781 (2013).
20. Niu, S. *et al.* Theory of sliding-mode triboelectric nanogenerators. *Adv. Mater.* **25**, 6184–6193 (2013).
21. Lin, Z. H., Cheng, G., Lee, S., Pradel, K. C. & Wang, Z. L. Harvesting water drop energy by a sequential contact-electrification and electrostatic-induction process. *Adv. Mater.* **26**, 4690–4696 (2014).
22. Wang, Z. *et al.* Ultrahigh electricity generation from low-frequency mechanical energy by efficient energy management. *Joule* **5**, 441–455 (2021).
23. Liu, Y. *et al.* Quantifying contact status and the air-breakdown model of charge-excitation triboelectric nanogenerators to maximize charge density. *Nat. Commun.* **11**, 1599 (2020).
24. Zhu, G. *et al.* Harvesting water wave energy by asymmetric screening of electrostatic charges on a nanostructured hydrophobic thin-film surface. *ACS Nano* **8**, 6031–6037 (2014).
25. Yang, X., Chan, S., Wang, L. & Daoud, W. A. Water tank triboelectric nanogenerator for efficient harvesting of water wave energy over a broad frequency range. *Nano Energy* **44**, 388–398 (2018).
26. Vourdas, N., Tserepi, A. & Gogolides, E. Nanotextured super-hydrophobic transparent poly (methyl methacrylate) surfaces using high-density plasma processing. *Nanotechnology* **18**, 125304 (2007).
27. Nahian, S. A., Cheedarala, R. K. & Ahn, K. K. A study of sustainable green current generated by the fluid-based triboelectric nanogenerator (FluTENG) with a comparison of contact and sliding mode. *Nano Energy* **38**, 447–456 (2017).

28. Cheedarala, R. K., Duy, L. C. & Ahn, K. K. Double characteristic BNO-SPI-TENGs for robust contact electrification by vertical contact separation mode through ion and electron charge transfer. *Nano Energy* **44**, 430–437 (2018).
29. Cheng, X. *et al.* Characterization of catalysts and membrane in DMFC lifetime testing. *Electrochim. Acta* **51**, 4620–4625 (2006).
30. Moynihan, R. E. The molecular structure of perfluorocarbon polymers. Infrared studies on polytetrafluoroethylene[1]. *J. Am. Chem. Soc.* **81**, 1045–1050 (1959).
31. Kaur, N. *et al.* Effective energy harvesting from a single electrode based triboelectric nanogenerator. *Sci. Rep.* **6**, 38835 (2016).
32. Weng, R., Zhang, H. & Liu, X. Spray-coating process in preparing PTFE-PPS composite super-hydrophobic coating. *AIP Adv.* **4**, 031327 (2014).
33. Scarratt, L. R. J., Hoatson, B. S., Wood, E. S., Hawkett, B. S. & Neto, C. Durable superhydrophobic surfaces via spontaneous wrinkling of teflon AF. *ACS Appl. Mater. Interfaces* **8**, 6743–6750 (2016).
34. Pieter, V. W. & Ullrich, S. Super-hydrophobic surfaces made from Teflon. *Soft Matter* **3**, 426–429 (2007).
35. Cheedarala, R. K., Parvez, A. N. & Ahn, K. K. Electric impulse spring-assisted contact separation mode triboelectric nanogenerator fabricated from polyaniline emeraldine salt and woven carbon fibers. *Nano Energy* **53**, 362–372 (2018).
36. Cheedarala, R. K. & Song, J. I. In situ generated hydrophobic micro ripples via π–π stacked pop-up reduced graphene oxide nanoflakes for extended critical heat flux and thermal conductivity. *RSC Adv.* **9**, 31735–31746 (2019).
37. Kong, K. *et al.* Electrical thermal heating and piezoresistive characteristics of hybrid CuO–woven carbon fiber/vinyl ester composite laminates. *Compos. Part A: Appl. Sci. Manuf.* **85**, 103–112 (2016).
38. van der Wal, P. & Steiner, U. Super-hydrophobic surfaces made from Teflon. *Soft Matter* **3**, 426–429 (2007).
39. Li, H., Wang, R., Hu, H. & Liu, W. Surface modification of self-healing poly(urea-formaldehyde) microcapsules using silane-coupling agent. *Appl. Surf. Sci.* **255**, 1894–1990 (2008).
40. Larrieu, J., Held, B., Martinez, H. & Tison, Y. Ageing of atactic and isotactic polystyrene thin films treated by oxygen DC pulsed plasma. *Surf. Coat. Technol.* **200**, 2310–2316 (2005).
41. Cheedarala, R. K., Shahriar, M., Ahn, J. H., Hwang, J. Y. & Ahn, K. K. Harvesting liquid stream energy from unsteady peristaltic flow induced pulsatile flow-TENG (PF-TENG) using slipping polymeric surface inside elastomeric tubing. *Nano Energy* **65**, 104017 (2019).
42. Pletincx, S. *et al.* Unravelling the chemical influence of water on the PMMA/aluminum oxide hybrid interface in situ. *Sci. Rep.* **7**, 13341 (2017).
43. Cheedarala, R. K., Park, E. J., Park, Y. B. & Park, H. W. Highly wettable CuO: graphene oxide core–shell porous nanocomposites for enhanced critical heat flux. *Phys. Status Solidi A* **212**, 1756–1766 (2015).
44. Cheedarala, R. K., Park, E., Kong, K., Park, Y. B. & Park, H. W. Experimental study on critical heat flux of highly efficient soft hydrophilic CuO–chitosan nanofluid templates. *Int. J. Heat. Mass. Transf.* **100**, 396–406 (2016).
45. Cheedarala, R. K., Jeon, J. H., Kee, C. D. & Oh, I. K. Bio-inspired all-organic soft actuator based on a π–π stacked 3D ionic network membrane and ultra-fast solution processing. *Adv. Funct. Mater.* **24**, 005–6015 (2014).
46. Jeon, J. H., Cheedarala, R. K., Kee, C. D. & Oh, I. K. Dry-type artificial muscles based on pendent sulfonated chitosan and functionalized graphene oxide for greatly enhanced ionic interactions and mechanical stiffness. *Adv. Funct. Mater.* **23**, 6007–6018 (2013).
47. Joseph, P. & Tabeling, P. Direct measurement of the apparent slip length. *Phys. Rev. E* **71**, 035303 (2005).
48. Joly, L., Ybert, C., Trizac, E. & Bocquet, L. Hydrodynamics within the electric double layer on slipping surfaces. *Phys. Rev. Lett.* **93**, 257805 (2004).
49. Elabbasi, N., Bergstrom, J. & Brown, S. Fluid–structure interaction analysis of a peristaltic pump. In *Proceedings of the 2011 COMSOl Conference*, Boston, USA.
50. Bolt, G. H. Analysis of the validity of the Gouy–Chapman theory of the electric double layer. *J. Colloid Sci.* **10**, 206–218 (1955).
51. Lungu, M. Electrical separation of plastic materials using the triboelectric effect. *Miner. Eng.* **17**, 69–75 (2004).
52. Kazban, R. V. & Mason, J. J. Fluid mechanics approach to machining at high speeds: Part I: justification of potential flow models. *Mach. Sci. Technol.* **11**, 475–489 (2007).
53. Fan, B., Bhattacharya, A. & Bandaru, P. R. Enhanced voltage generation through electrolyte flow on liquid-filled surfaces. *Nat. Commun.* **9**(1–7), 1–7 (2018).
54. Park, H. & Choa, S. H. Measurement of liquid flow rate by self-generated electrokinetic potential on the microchannel surface of a solid. *Sens. Actuators A Phys.* **208**, 88–94 (2014).
55. Berg, J. M. & Dallas, T. *Peristaltic Pumps. Encyclopedia of Microfluidics and Nanofluidics, Chap. 2* (Springer, 2014).
56. Cheedarala, R. K. & Song, J. I. Face-centred cubic CuO nanocrystals for enhanced pool-boiling critical heat flux and higher thermal conductivities. *Int. J. Heat Mass Transf.* **162**, 120391 (2020).
57. Wang, Z. L. & Wang, A. C. n the origin of contact-electrification. *Mater. Today* **30**, 34–51 (2019).
58. Cheedarala, R. K. & Song, J. I. Sand-polished Kapton film and aluminum as source of electron transfer triboelectric nanogenerator through vertical contact separation mode. *Int. J. Smart Nano Mater.* **11**, 38–46 (2020).
59. Cheedarala, R. K. & Song, J. I. Ionic polymer-metal composite electro-active nano-biopolymer actuator. In *23rd International Conference on Mechatronics Technology (ICMT)*, Salerno, Italy, 1–4 (2019). https://doi.org/10.1109/ICMECT.2019.8932104.
60. Cheedarala, R. K. & Song, J. I. Moderately transparent chitosan-PVA blended membrane for strong mechanical stiffness and as a robust bio-material energy harvester through contact-separation mode TENG. *Front. Nanotechnol.* **3**, 667453 (2021).
61. Chidarala, R. K., Prabhakar, M. N., Gon Cho, B., Park, Y. B. & Song, J. I. Novel 3D-networked melamine-naphthalene-polyamic acid nanofillers doped in vinyl 2 ester resin for higher flame retardancy. *Mater. Adv.* **2**, 4339–4351 (2021).
62. Cheedarala, R. K. & Song, J. I. Ionic polymer-metal composite electro-active nano-biopolymer actuator. *J. Mech. Eng. Autom.* **9**, 225–229 (2019).
63. Thomas, S. *et al.* Thermal, mechanical and biodegradation studies of biofiller based poly-3-hydroxybutyrate biocomposites. *Int. J. Biol. Macromol.* **155**, 1373–1384 (2020).
64. Cheedarala, R. K., Chidambaram, R. R., Siva, A. & Song, J. I. An aerobic oxidation of alcohols into carbonyl synthons using bipyridyl-cinchona based palladium catalyst. *RSC Adv.* **11**, 32942–32954 (2021).
65. Cheedarala, R. K. & Song, J. I. Integrated electronic skin (e-Skin) for harvesting of TENG energy through push-pull ionic electrets and ion-ion hopping mechanism. *Sci. Rep.* https://doi.org/10.21203/rs.3.rs-1070606/v1 (2021).
66. Hughes, C., Yeh, L.-H. & Qian, S. Field effect modulation of surface charge property and electroosmotic flow in a nanochannel: Stern layer effect. *Phys. Chem. C* **117**, 9322–9331 (2013).
67. Peristaltic pump dispensing. https://motion.schneider-electric.com/success-stories/peristaltic-pumps/GoogleScholar.
68. Chaitanya, S., Cheedarala, R. K. & Song, J. I. Microwave-synthesized Mg+ 2 doped jute fibers and their application as a reinforcement in biocomposites. *Compos. Part B Eng.* **197**, 108154 (2020).

Acknowledgements

This work was supported by the National Research Foundation of Korea (NRF) grant funded by the Korea government (MSIP) No. 2017R1A2B2011730, No. 2018R1A6A1A03024509 and 2019R1A2C1011113.

Author contributions

The conception, design, experiments, analysis, manuscript writing and review: R.K.C., Institutional facilities and funding source: J.I.S.

Competing interests

The authors declare no competing interests.

Additional information

Supplementary Information The online version contains supplementary material available at https://doi.org/10.1038/s41598-022-07614-5.

Correspondence and requests for materials should be addressed to R.K.C. or J.I.S.

Reprints and permissions information is available at www.nature.com/reprints.

Publisher's note Springer Nature remains neutral with regard to jurisdictional claims in published maps and institutional affiliations.